Chemical Engineering Journal 452 (2023) 138938

Contents lists available at ScienceDirect

Chemical Engineering Journal

journal homepage: www.elsevier.com/locate/cej

# Boosting oxygen reduction with coexistence of single-atomic Fe and Cu sites decorated nitrogen-doped porous carbon

Heng Liu [a,1], Luozhen Jiang [b,1], Yamin Wang [c,1], Xinxin Wang [a], Javid Khan [a], Yanlin Zhu [a], Jiamin Xiao [a], Lina Li [b,*], Lei Han [a,*]

[a] College of Materials Science and Engineering, Hunan Joint International Laboratory of Advanced Materials and Technology for Clean Energy, Hunan University, Changsha, Hunan 410082, People's Republic of China
[b] Shanghai Synchrotron Radiation Facility, Shanghai Advanced Research Institute, Shanghai, People's Republic of China
[c] Department of Chemistry, Guangdong Provincial Key Laboratory of Catalysis, Southern University of Science and Technology, Shenzhen, Guangdong 518000, People's Republic of China

ARTICLE INFO

*Keywords:*
Dual-metal single atomic site
Metal foam
Oxygen reduction reaction

ABSTRACT

Rational design of iron-nitrogen-carbon (Fe-N-C) oxygen reduction reaction (ORR) catalysts simultaneously increasing the intrinsic activity and density of active site remains a huge challenge. Herein the coexistence of single-atomic Fe and Cu sites decorated nitrogen-doped porous carbon has been successfully fabricated by hydrothermal synthesis of Fe, Cu co-doped ZIF-8 in the presence of Fe and Cu foam with subsequent $NH_3$ pyrolysis. The X-ray absorption spectra confirmed the atomically dispersed Fe and Cu species with Fe-$N_4$ and Cu-$N_4$ coordination structures in the resultant FeCu SACs/NC catalyst. Meanwhile, the introduction of Cu has been experimentally and theoretically demonstrated to modulate the electronic structure of Fe active sites during the desorption of *OH intermediate process, as well as increase the density of Fe active sites, thereby effectively enhancing the intrinsic activity and selectivity toward the ORR.

## 1. Introduction

Development of highly efficient oxygen reduction reaction (ORR) catalyst has shown a vital role in promoting the large-scale commercial application of fuel cells. Currently, the commercial ORR catalysts are focused on platinum (Pt)-based materials with the intrinsic shortcomings of prohibitive cost and unsatisfactory durability [1,2]. Therefore, it is of importance yet remains a challenge to explore inexpensive and high-performance non-noble-metal ORR catalysts. In this regard, nanostructured metal-nitrogen-carbon (M-N-C) materials have received increasing attentions due to facile preparation and outstanding catalytic performance [3,4]. Especially, transition-metal-based single-atom catalysts (SACs) have been widely investigated and explored in various fields owing to their utmost atom utilization efficiency, controllable electronic structures, and superior performance [5–10]. Moreover, single-atomic transition metal-nitrogen ($M\text{-}N_x$) coordinated species within M-N-C materials have been demonstrated as dominant catalytically active sites to promote the ORR process from an experimental and theoretical perspective [10,11]. Very recently, Strasser's group pointed out the future direction toward the improvement in the ORR performance from the viewpoint of the density and intrinsic turnover frequency of active metal sites [12]. Indeed, these two aspects are exactly what researchers are pursuing now, and considerable efforts have been made to achieve the enhancement in the ORR performance of transition-metal-based SACs through the introduction of second type of metal atoms [13–18] and/or non-metal heteroatoms (S, P) [19–21] to modulate the electronic structure and geometry configuration of active sites and optimize their binding strength toward the reaction intermediates (e.g. *$O_2$, *OOH, *OH, and *O) [22–24], thus leading to the improvement in the intrinsic activity. Despite this, there is still some room for improving their performance in catalytic activity and durability relative to commercial Pt/C catalysts. Besides, the reported preparation methods of transition-metal SACs, including atomic layer deposition [25], immersion method [26], and co-precipitation [27], have some disadvantages such as low efficiency, high cost, and complicated synthesis process. In addition, most of research work focuses on improving the ORR performance from one of the two aspects mentioned above, that is, increasing the intrinsic activity or the density of metal active sites. In

* Corresponding authors.
*E-mail addresses:* lilina@sinap.ac.cn (L. Li), hanlei@hnu.edu.cn (L. Han).
[1] These authors contributed equally to this work.

https://doi.org/10.1016/j.cej.2022.138938
Received 8 July 2022; Received in revised form 23 August 2022; Accepted 27 August 2022
Available online 2 September 2022

contrast, simultaneously achieving the optimization in intrinsic activity and density of metal active sites by a facile and efficient synthetic method has been seldom reported and remains challenge.

On the other hand, Fe-N-C catalysts show promising potential among various M-N-C materials, since the foreign electrons accommodated into the 3d unoccupied orbitals of active Fe center could be readily penetrated into the anti-bonding π orbital of oxygen and facilitate the fast displacement of $O_2/OH^-$ and $OH^-$ regeneration, thus resulting in the high ORR activity [28–39]. Nevertheless, Fe-N-C catalysts also face some issues in the activity and durability owing to the following two reasons: (1) the strong bonding between the active Fe sites and the reaction intermediates (*OOH and *OH) is detrimental for the desorption process, thus causing the slow reaction kinetics during the overall ORR process [35]. (2) the produced $H_2O_2$ during the ORR process can react with the active Fe sites to generate the reactive oxygen-containing free radicals, which induces the oxidation degradation of carbon support as well as the proton exchange membranes if application in practical PEMFCs [3,40,41]. In order to solve these problems, the introduction of second metal has been considered to be an efficient way to inhibit the $H_2O_2$ production during the ORR process. Meanwhile, the electronegativity difference between Fe and second metal could also induce the electron transfer between them, thus optimizing the electronic structures of Fe and the bonding strength between the reaction intermediates and active Fe sites [42–44].

Based on the considerations above, dual-metal SACs with the coexistence of single-atomic Fe and Cu decorated nitrogen-doped porous carbon matrix (noted as FeCu SACs/NC) as ORR catalysts have been successfully prepared through the synthesis of Fe, Cu co-doped ZIF-8 in the presence of Fe and Cu foam followed by the subsequent pyrolysis under the $NH_3$ atmosphere. The extended X-ray absorption fine structure spectra (EXAFS) confirmed the formation of single-atomic Fe and Cu sites with via Fe-$N_4$ and Cu-$N_4$ coordination bonds affixed to the carbon matrix, indicating the successful constrcution of dual-metal SACs through the simultaneous addition of Fe and Cu foam. Moreover, the introduction of Cu foam was also found to greatly promote the escape of Fe atoms from the bulk Fe foam, thus increasing the density of single-atomic Fe sites. Benefiting from the synergistic effect between the interaction of single-atom Fe and Cu sites and the increased density of Fe sites, the resultant FeCu SACs/NC catalyst exhibits comparable ORR performance to Pt/C as well as good methanol tolerance and stability. In addition, it also exhibits excellent performance in Zn-air batteries with a maximum power density of 153 mW $cm^{-2}$ and long-term stability.

## 2. Experimental procedures

### 2.1. Material synthesis

Prior to the use of metal foam, the Fe and Cu foam (2 cm × 1 cm) were firstly cleaned with 1 M HCl under the assistance of ultrasonication for 20 min to remove the surface oxide layer, and washed with $H_2O$ and ethanol. 2 mmol $Zn(NO_3)_2{\cdot}6H_2O$ dissolved in 15 mL methanol mixed with 10 mmol 2-methylimidazole dissolved in 15 mL methanol, and then was transferred with Fe and Cu foam to a 100 mL stainless-steel Teflon-lined autoclave and heated in an electric oven at 140 °C for 6 h. After cooling to room temperature, the resultant precipitate was collected and subsequently rinsed with ethanol, and dried in oven at 80 °C (FeCu-ZIF-8). The dried sample was heated to 950 °C with the heating rate 5 °C/min in an Ar atmosphere, and then kept at 950 °C for 3 h in a $NH_3$/Ar atmosphere, which was named as FeCu SACs/NC. The Fe SACs/NC, Cu SACs/NC, and NC were prepared at the same conditions with only addition of Fe foam, Cu foam, and no added, respectively.

### 2.2. Electrochemical measurements

5 mg of catalysts powder was ultrasonically dispersed in the mixture of ethanol-$H_2O$ (1 mL, v/v = 1:1) containing 50 μL of 5 wt % Nafion solution. Then, 40 μL of the catalyst ink was loaded onto a glassy carbon electrode (D = 5.6 mm) of a rotation ring-disk electrode (RRDE) with a catalyst loading of 0.8 mg $cm^{-2}$ as working electrode. For comparison, commercial 20 wt % Pt/C ink was prepared by the same method. All electrochemical measurements were carried on a CHI 760E electrochemical workstation. Graphite rod and Ag/AgCl ($KNO_3$-saturated) were used as counter electrode and reference electrode, respectively. The number of electron transferred (n) and kinetic current density ($J_k$) were calculated from the Koutecky-Levich equation:

$$\frac{1}{J}=\frac{1}{J_L}+\frac{1}{J_K}=\frac{1}{B\omega^{1/2}}+\frac{1}{J_K} \quad (1)$$

$$B = 0.62nFC_0D^{2/3}\upsilon^{-1/6} \quad (2)$$

where J is the measured current; $J_L$ is the diffusion limiting current; ω is the angular velocity of the disk; F is the Faraday constant (96485 C $mol^{-1}$); $C_0$ is the bulk concentration of oxygen ($1.2 \times 10^{-6}$ mol $cm^{-1}$); $D_0$ is the diffusion coefficient of oxygen ($1.9 \times 10^{-5}$ $cm^2$ $s^{-1}$); υ is the he kinetic viscosity (0.01 $cm^2$ $s^{-1}$); n is the number of electron transferred during the ORR process.

The n can also be calculated from the RRDE measurement according to the following equation:

$$n = 4 \times \frac{I_{disk}}{I_{disk}+I_{ring}/N} \quad (3)$$

where $I_{disk}$ is the measured current of disk electrode; $I_{ring}$ is the measured current of Pt ring electrode; N is the current collection efficiency of Pt ring.

### 2.3. Zn-air battery test

Air cathode was first prepared by spraying the catalyst onto carbon paper with the mass loading of 2.0 mg $cm^{-2}$ and then was assembled with a Zn foil anode. 6 M KOH + 0.2 M $Zn(CH_3COO)_2$ solutions was employed as electrolyte. Meanwhile, button-like all-solid-state zinc–air battery was also constructed using hydrogel polymer as electrolyte instead of KOH. Typically, 2 g of PVA was first dissolved in 20 mL of deionized water at 90 °C under magnetic stirring for 1 h to form a uniform solution. Then, 30 mL of graphene oxide solution (1 mg $mL^{-1}$) was gradually added to pre-prepared PVA solution and kept at 90 °C for 3 h under vigorous stirring. Afterwards, the resultant mixture was cast onto a clean container and then kept it at 70 °C. Finally, the resultant product was cut into round shape (D = 18 mm) and immersed in 6 M KOH + 0.2 M $Zn(CH_3COO)_2$ solutions for 24 h.

## 3. Results and discussion

### 3.1. Structural characterization of the catalysts

The typical preparation illustration of FeCu SACs/NC catalyst is schemed in Fig. 1A. Considering the fact that metal atoms can diffuse out from the bulk metal under high temperature and pressure, Fe and Cu foam were selected as metal sources to prepare the Fe, Cu dual-doped ZIF-8 (noted as FeCu-ZIF-8) through the hydrothermal reaction between $Zn^{2+}$ and 2-methylimidazole in the presence of Fe and Cu foam. Subsequently, FeCu SACs/NC catalysts were obtained through the pyrolysis under $NH_3$ atmosphere. As shown, the resultant FeCu SACs/NC catalyst exhibited the uniform polyhedral shape with an average size of around 110 nm (Fig. 1B-C). High-resolution TEM image verifies the no formation of obvious crystalline metal nanoparticles or clusters within the carbon matrix (Fig. 1D), and similar results were also observed with the Cu SACs/NC and Fe SACs/NC (Fig. S1 and S2). The high-angle annular dark-field scanning transmission electron microscopy (HAADF-STEM) images and element mappings revealed the uniform distribution of C, N, Fe, and Cu within the resultant FeCu SACs/NC

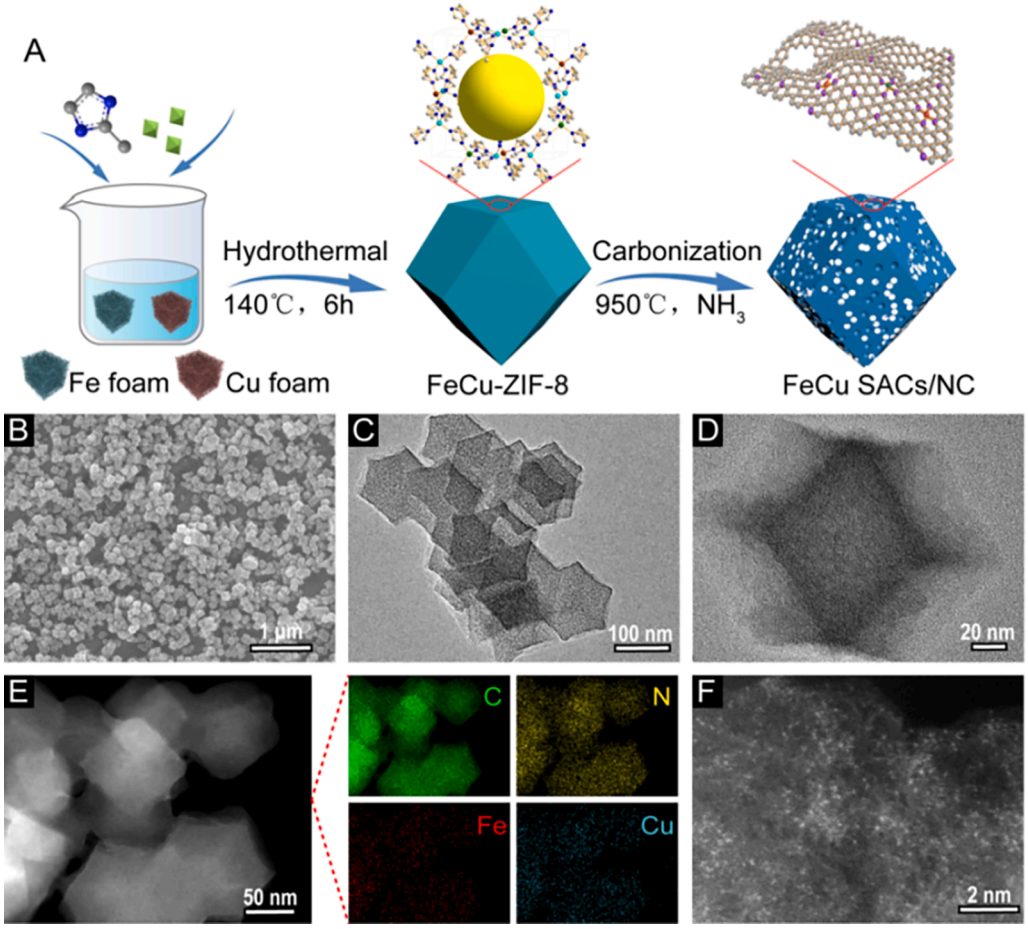


**Fig. 1.** (A) The preparation scheme of FeCu SACs/NC catalyst. (B) FESEM, (C) TEM, (D) HRTEM, (E) HAADF-STEM and the corresponding EDS mappings, and (F) aberration-corrected HAADF-STEM images of the FeCu SACs/NC.

catalyst (Fig. 1E), and the presence of atomically dispersed Fe and Cu species can be proved by the aberration-corrected HAADF-STEM image, where obvious individual Fe and Cu atoms could be observed (Fig. 1F). Moreover, X-ray diffraction (XRD) patterns (Fig. S3A) revealed that there are only two broad peaks at 25° and 44° for all the resultant catalysts corresponding to the (0 0 2) and (1 0 1) crystal plane of graphitic carbon, respectively, whereas no peaks belonging to crystalline Fe and/or Cu-based metallic or metallic carbide nanoparticles were observed [45,46].

All the resultant catalysts exhibited the similar Raman spectra with the almost same intensity ratio of D band at 1587 $cm^{-1}$ and G band at 1344 $cm^{-1}$ (Fig. S3B), which may be due to the relatively low amount of Fe and Cu (Table S1) [47,48]. Meanwhile, the increased content of Fe (0.67 wt %) could be observed within the resultant FeCu SACs/NC catalyst after the introduction of Cu compared to that of the resultant Fe SACs/NC catalyst (0.11 wt %). Further, we analyzed the content of Fe ions in the solution of FeCu-ZIF-8 (1.4 mg/L) (Table S2), which is twice higher than that in Fe-ZIF-8 (0.7 mg/L), clearly demonstrating that the introduction of Cu foam can greatly promote the Fe atoms escape from the bulk foam structure to increase the concentration of Fe ions. In addition, we also increased the amount of raw materials ($Zn(NO_3)_2{\cdot}6H_2O$ and 2-methylimidazole) by two times during the hydrothermal process, and found that the content of Fe ions increase accordingly to 3.2 mg/L. This phenomenon could be explained by the following facts: (1) $Zn(NO_3)_2{\cdot}6H_2O$ containing crystal water provides an acidic environment and can react with Fe foam to produce $Fe^{2+}$ and $Fe^{3+}$ ions because of the presence of oxygen in the reaction system, which then reacts Cu foam to produce $Cu^{2+}$ ions; (2) $M^0$ on metal foam would transfer electrons to the dangling nitrogen groups on ZIF-8 to produce $M^{\delta+}$ ($0 < \delta < 3$) species such as $Fe^{2+}$ and $Cu^{2+}$ ions, which then coordinates with the surface nitrogen dangling bonds of ZIF-8 to form M—N bonds [49]; (3) the produced $Cu^{2+}$ ions can also react with Fe foam to generate more $Fe^{2+}$ ions. $N_2$ sorption isotherm results demonstrated that though the optimal FeCu SACs/NC catalyst exhibited the smallest BET surface area (649.7 $m^2\ g^{-1}$), its pore size distribution mainly centered at around 0.5–2.0 nm belonging to micropore, which may provide more anchoring sites for catalytically active Fe/Cu sites (Fig. S4) [50].

The elemental composition and chemical state of the resultant catalysts were investigated by X-ray photoelectron spectroscopy (XPS). For the high-resolution XPS spectrum of C 1 s, there are three fitted peaks at 284.8 eV, 285.6 eV, and 289.3 eV, which could belong to C—C/C═C, C—N, and C═O, respectively (Fig. S5A and S6) [51]. The high-resolution XPS spectrum of N 1 s (Fig. S5B) demonstrated that the dominant nitrogen species are composed of pyridinic-N (398.5 eV), Fe/Cu-$N_x$ (399.2 eV), pyrrolic-N (400.0 eV), graphitic-N (401.1 eV), and oxidized-N (402.9 eV), respectively [52–54]. Two main peaks at 709.6 eV and 713.1 eV in the high-resolution XPS spectrum of Fe 2p correspond to $Fe^{2+}$ and $Fe^{3+}$ of Fe $2p_{3/2}$, respectively (Fig. S5C) [55,56]. The high-resolution XPS spectrum of Cu 2p can be also divided into two peaks at 936.1 eV and 932.4 eV (Fig. S5D), which can be assigned to $Cu^{2+}$ and $Cu^{+}$ [57]. Furthermore, the surface atomic contents of the resultant catalysts were summarized in Table S3, and the resultant FeCu SACs/NC catalyst contain higher content of Fe (0.43 at%) and Cu (0.16 at%) than the resultant Fe SACs/NC catalyst (0.15 at %) and Cu SACs/NC catalyst (0.13 at%), which was consistent with the ICP-MS results.

The detailed structural information of the atomically dispersed Fe and Cu active sites within the resultant catalysts, including the local

coordination environment and the valence state, were further identified by the X-ray absorption near-edge structure (XANES) and extended X-ray absorption fine structure (EXAFS). The Fe K-edge XANES spectra (Fig. 2A) revealed that the near-edge absorption position of the resultant FeCu SACs/NC and Fe SACs/NC located between those of the standard Fe foil, iron phthalocyanine (FePc), $Fe_3O_4$ and $Fe_2O_3$, implying that the average valence state of Fe should be slightly lower than + 2. Besides, both FeCu SACs/NC and Fe SACs/NC show clear pre-edge peaks at 7113.1 eV, which are similar to the characteristics of FePc, suggesting the typical Fe-N coordination structure [58]. Interestingly, the positive shift of the near-edge absorption position for the resultant FeCu SACs/NC was observed compared to the resultant Fe SACs/NC, displaying the more positive valence state of Fe in the resultant FeCu SACs/NC. Similarly, the Cu K-edge XANES spectra also presented that the average valence states of Cu within the resultant FeCu SACs/NC and Cu SACs/NC are both close to + 2 according to the shift of the near-edge absorption position (Fig. 2B), whereas the resultant FeCu SACs NC possessed the lower valence state of Cu compared to the resultant Cu SACs/NC. This result demonstrated that the charge transfer between Fe and Cu within the resultant FeCu SACs/NC may lead to the increase of valence state of Fe and the decrease of valence state of Cu, respectively. The Fe and Cu K-edge EXAFS spectra in R-space (Fig. 2C-D) revealed a primary peak at ca. 1.50 Å assigned to Fe-N and Cu–N scattering path. Furthermore, the EXAFS fitting curves and the corresponding fitting results (Fig. 2E and Table S4) confirmed that the average coordination numbers of Fe-N and Cu–N are about 4, suggesting the formation of the well-defined Fe-$N_4$ and Cu-$N_4$ moieties in the resultant FeCu SACs/NC catalyst (Fig. 2F). Similar results were also observed for the resultant Fe SACs/NC and Cu SACs/NC catalyst (Fig. S7 and Table S4). Moreover, compared to the resultant Fe SACs/NC, the Fe sites in resultant FeCu SACs/NC catalyst possess a higher valence with closer to + 2, which were reported to be the dominant ORR active sites [59].

### 3.2. Catalytic performance of the resultant catalysts for ORR

The ORR performance of the resultant catalysts was further investigated with the typical three-electrode configuration by rotating disk electrode (RDE) technique. A significant redox peak with the most positive potential could be observed in the presence of $O_2$ for the resultant FeCu SACs/NC catalyst (Fig. S8). The resultant FeCu SACs/NC catalyst also exhibited the enhanced ORR activity with the onset potential ($E_{onset}$) of 0.84 V, the half-wave potential ($E_{1/2}$) of 0.75 V, and a kinetic current density at 0.7 V ($J_k$) of 7.27 mA $cm^{-2}$, which are superior to the resultant NC (0.58 V, 0.39 V, 0.01 mA $cm^{-2}$), Fe SACs/NC (0.78 V, 0.71 V, 4.27 mA $cm^{-2}$), Cu SACs/NC (0.68 V, 0.55 V, 0.14 mA $cm^{-2}$), and only show the slight negative shift of 40 mV in $E_{1/2}$ relative to commercial Pt/C (0.79 V) (Fig. 3A, B). The catalytic performance of FeCu SACs/NC is comparatively better than many of the reported M-N-C catalysts in acidic (Table S5). The Tafel slope of the FeCu SACs/NC was measured to be 89.1 mV $dec^{-1}$, which is lower than the values for the Fe SACs/NC, Cu SACs/NC, NC and Pt/C (96.6, 168.4, 253.5 and 112.6 mV $dec^{-1}$) (Fig. 3C), indicating that its electron transfer rate is much faster. The Koutecky-Levich (K-L) plots, derived from the linear sweep voltammetry curves at different rotating speeds, showed a good linear relationship, indicating the first-order reaction kinetics (Fig. 3D and S9). Moreover, the calculated number of electron transferred of 3.86 implied the dominant direct four-electron ORR pathway over the resultant FeCu SACs/NC catalyst. Besides, the average number of electron transferred and the $H_2O_2$ selectivity were also determined to be 3.95 and below 2.6 % by rotating ring-disk electrode (RRDE) technique, which is smaller than that of the resultant Fe SACs/NC catalyst (6.1 %) (Fig. 3E). This result demonstrated that the introduction of Cu-$N_4$ moieties can efficiently suppress the $H_2O_2$ production during the ORR process, which can be further confirmed by the lower $H_2O_2$ selectivity of the resultant Cu SACs/NC catalyst (1.9 %). Further, methanol tolerance was also evaluated by means of chronoamperometric at 0.7 V upon the addition of 2.0 M methanol. No obvious change in the ORR current for the resultant FeCu SACs/NC catalyst was observed after the addition of methanol, whereas a sharp decrease was observed for Pt/C (Fig. S10), indicating the remarkably superior methanol tolerance of the resultant FeCu SACs/NC catalyst. Meanwhile, the long-term stability of FeCu SACs/NC and Pt/C are further evaluated by chronoamperometric at 0.7 V. The current density remains above 89 % for the resultant FeCu SACs/NC catalyst after 10 h whereas dropping significantly to 80 % for Pt/C (Fig. 3F). In

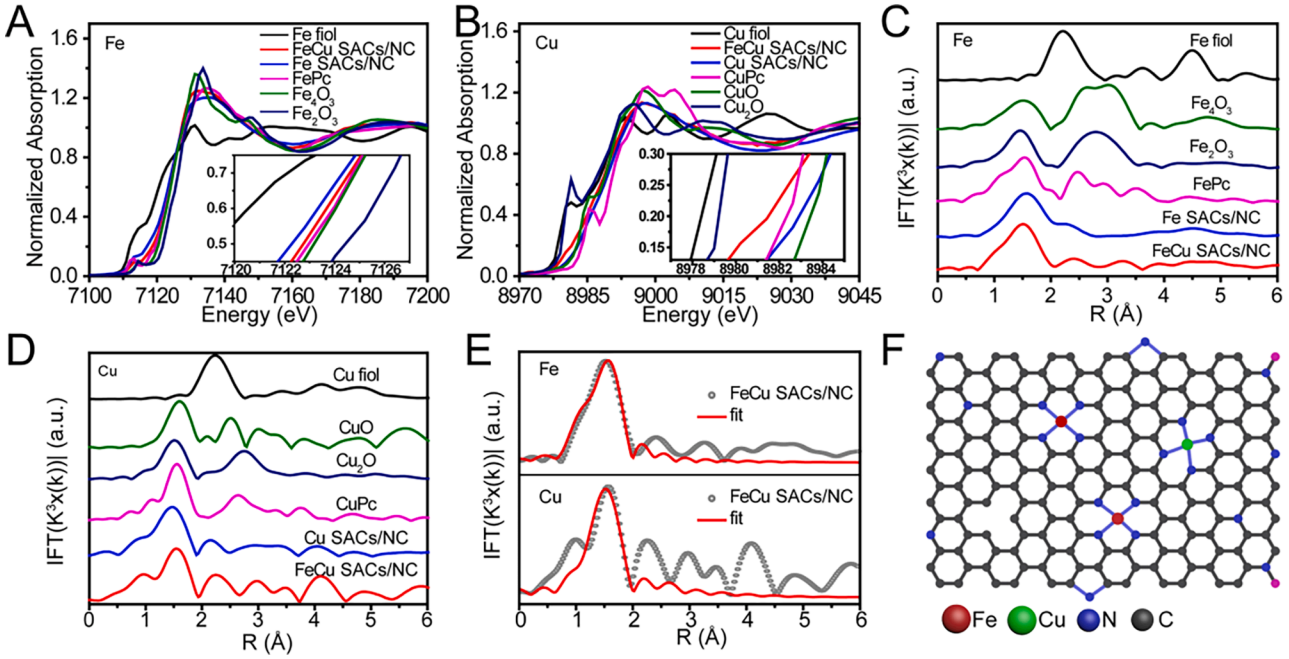


**Fig. 2.** (A) Fe K-edge XANES and (B) Cu K-edge XANES spectra. (C) Fourier transforms of EXAFS spectra of FeCu SACs/NC, Fe SACs/NC at Fe K-edge. (D) Fourier transforms of EXAFS spectra of FeCu SACs/NC, Cu SACs /NC at Cu K-edge. (E) EXAFS fitting curve for FeCu SACs /NC for Fe and Cu. (F) Schematic illustration of atomic dispersion structural model of Fe and Cu active sites.

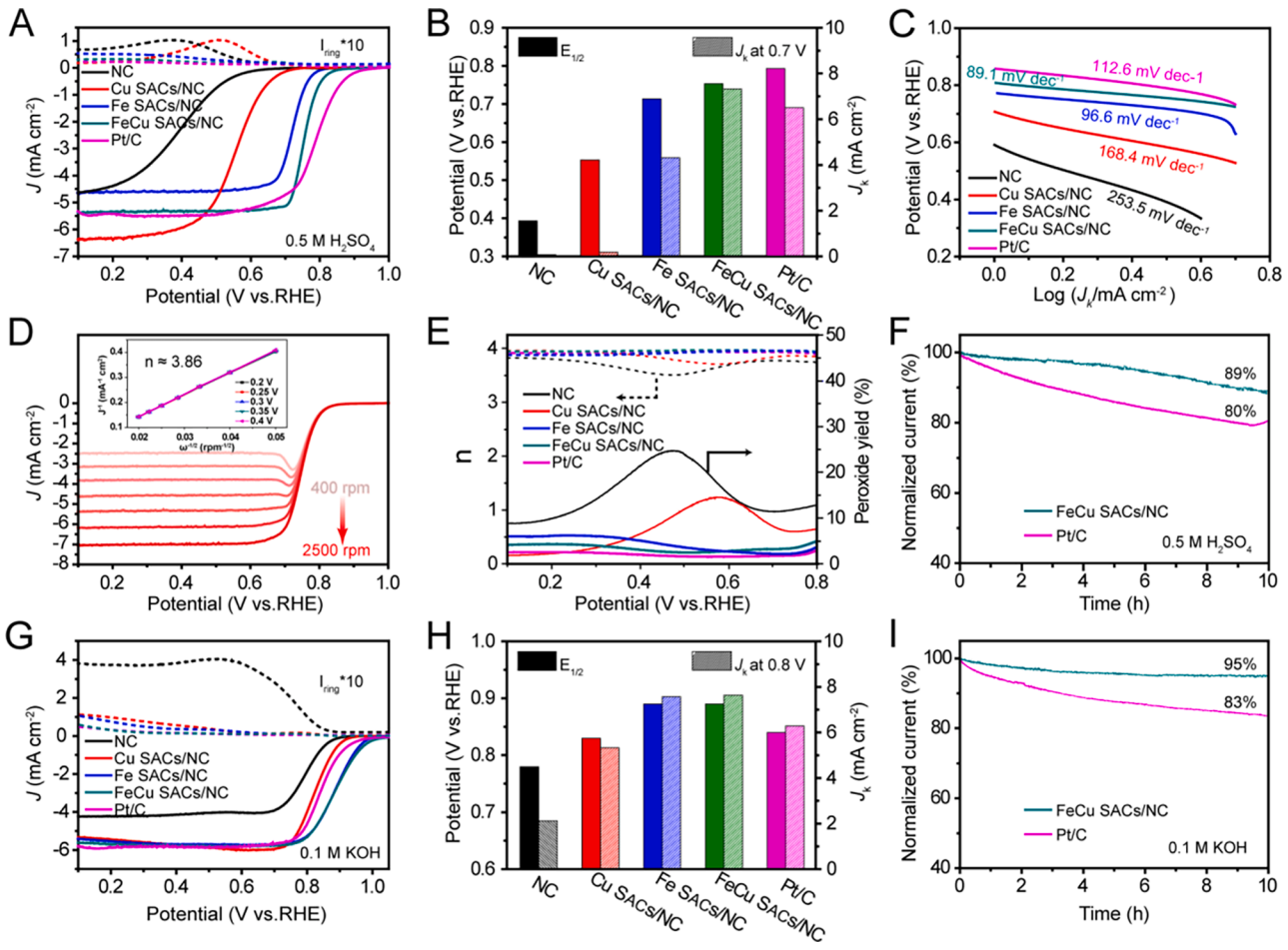


**Fig. 3.** (A) Linear sweep voltammetry (LSV) curves, (B) the corresponding $E_{1/2}$ and $J_k$, (C) Tafel slopes of the resultant catalysts and Pt/C in 0.5 M $H_2SO_4$. (D) LSV curves of FeCu SACs/NC at various rotating speed rates. (E) The number of electron transferred (n) and $H_2O_2$ selectivity of the resultant catalysts. (F) Relative retention i-t curves at 0.7 V in 0.5 M $H_2SO_4$ for FeCu SACs/NC and Pt/C. (G) LSV curves, (H) the corresponding $E_{1/2}$ and $J_k$ of the resultant catalysts and Pt/C in 0.1 M KOH. (I) Relative retention i-t curves at 0.7 V in 0.1 M KOH for FeCu SACs/NC and Pt/C. Note: all the electrochemical measuremets were performed in $O_2$-saturated electrolyte solution at the rotation speed rate of 1600 rpm without special statement.

addition, the morphologic structure and chemical composition of the catalyst after the stability test were also further characterized. As shown in Fig. S11-S12, no obvious aggregation of metal nanoparticles can be observed on the surface of the resultant FeCu SACs/NC, and there are no changes in the content and valence states of Fe and Cu, indicating the good stability of the resultant FeCu SACs/NC catalyst. However, there is still a partial degradation of the performance, which may come from the intolerance of the active site of the MNC-type catalyst under acidic conditions, and a partial demetallation reaction [22]. In addition, the performance of catalysts prepared under different atmospheric and temperature of hydrothermal conditions was also investigated. Compared with the catalysts under $H_2$ and Ar conditions, the $E_{1/2}$ of the catalysts has been greatly improved after the ammonia treatment (Fig. S13), which may be ascribed to the local Lewis basicity of N-doped carbon around the single site [31]. We investigated the effect of hydrothermal reaction temperature and prepared the catalysts by changing the temperature at 100 °C or 180 °C, which were noted as FeCu SACs/NC-L and FeCu NP/NC. XRD and FESEM results demonstrated that FeCu SACs/NC-L exhibited a uniform polyhedral shape, and no peaks belonging to crystalline Fe and/or Cu-based metallic or metallic carbide nanoparticles were observed (Fig. S14). In contrast, there are obvious peaks belonging to crystalline Fe and Cu metals in FeCu NPs/NCs, and SEM also showed the presence of distinct carbon nanotube structure and nanoparticles. Meanwhile, we also measured their ORR performance of the resultant FeCu SACs/NC-L and FeCu NP/NC, which are both inferior to that of the resultant FeCu SACs/NC catalyst (Fig. S15).

In addition to acidic medium, we also investigated the ORR performance of the resultant catalysts in alkaline medium. Similarly, the resultant FeCu SACs/NC catalyst exhibited the obvious redox peak, and the superior ORR activity ($E_{onset}$: 1.03 V, $E_{1/2}$: 0.89 V, $J_k$: 7.63 mA $cm^{-2}$) to Pt/C (0.98 V, 0.84 V, 6.28 mA $cm^{-2}$), Fe SACs/NC (0.99 V, 0.89 V, 7.57 mA $cm^{-2}$), Cu SACs/NC (0.93 V, 0.83 V, 5.32 mA $cm^{-2}$), NC (0.89 V, 0.78 V, 2.12 mA $cm^{-2}$), and most of the recently reported M-N-C electrocatalysts in an alkaline electrolyte (Fig. S16, Fig. 3G–H and Table S6). Nevertheless, unlike in acidic medium, there is almost no difference of the ORR activity between the resultant FeCu SACs/NC and Fe SACs/NC catalysts, which may be due to the high ORR activity of metal-free nitrogen species such as pyridinic-N and graphitic-N under alkaline condition [22,60,61]. Similarly, the Tafel slope of the FeCu SACs/NC was measured to be 68.6 mV $dec^{-1}$, lower than the values of 77.2 mV $dec^{-1}$ for the Pt/C (Fig, S17). The linear relationships at different potentials were observed by the K-Lplots (Fig, S18), and the average number of electron transferred was determined by RRDE technique to be above 3.9 with similar $H_2O_2$ selectivity to Pt/C (Fig. S19), demonstrating a desired apparent four-electron ORR pathway over the resultant FeCu SACs/NC catalyst. Moreover, the resultant FeCu SACs/NC catalyst also exhibited the excellent methanol tolerance, and better long-term stability maintaining almost 95 % of current density after 10 h relative to Pt/C (83 %) (Fig. S20 and Fig. 3I).

### 3.3. Theoretical study

To understand the synergistic effect of FeCu sites on the ORR activity, density functional theory (DFT) calculations were performed to explore the free energy profiles of six different models for FeCu SACs/NC by varying the distance between Fe and Cu sites within the nitrogen doped graphene by the experimental structural characterization (Fig. 4A, Fig. S21 and S22). The free energy profiles of ORR on $FeN_4$ (Fe SACs/NC) and $CuN_4$ (Cu SACs/NC) are also shown for comparison. On $CuN_4$, the first electron transfer step (* $+O_2 + H^+ + e^- \rightarrow$ *OOH) is the rate-determining step (RDS) and possesses a very high free energy change of 1.08 eV (Fig. 4B), suggesting that $CuN_4$ is not an efficient catalyst for ORR. On $FeN_4$ the RDS is the last electron transfer step (*OH $+ H^+ + e^- \rightarrow$ * $+H_2O$), which requires a free energy change of 0.67 eV. In the case of binuclear site, the RDS on model 1 with Fe-Cu distance at 2.43 Å was same with $FeN_4$, while the reaction free energy was significantly reduced to 0.35 eV on Model 1, manifesting faster ORR kinetics (Fig. S23). While on Model 2 and Model 3 with relatively larger Fe-Cu distance, the reaction energies of the RDS are very close to that of $FeN_4$. These results demonstrate that the improvement of the ORR activity in FeCu SACs/NC may be explained by the formation of atomically dispersed FeCu pair sites with a closer distance, as shown in model 1. As discussed in the Free energy diagram, the desorption of *OH intermediate on Fe site (i.e. the hydrogenation of *OH intermediate) is the RDS and should control the overpotential. This indicates that the strongly binding *OH is detrimental for the desorption process, the catalysts with Model 1 structure exhibited the highest ORR activity due to the moderate *OH adsorption near the top of the volcano strength (Fig. 4C). The projected density of states (PDOS) of Fe atoms in Model 1 and $FeN_4$ were also explored to further confirm the vital role of Cu site in assisting $FeN_4$ site for boosting the ORR performance. Compared to Fe-$N_4$ active sites, an obvious shift of Fe-d orbitals in Model 1 indicates that the increased electrons fill into the antibonding orbitals of Fe atom (Fig. S24), thus weakening the interaction between adsorbed *OH and Fe-center and boosting the ORR process [62].

### 3.4. Zinc-air battery performance

To further demonstrate the applicability of FeCu SACs/NC, an assembled Zn-air battery was constructed using the FeCu SACs/NC electrocatalyst loaded on carbon paper as an air cathode, 6 M KOH solution with 0.2 M $Zn(CH_3COO)_2$ as an electrolyte, and Zn plate as an anode, respectively. Such FeCu SACs/NC-based Zn-air battery exhibited a high open circuit potential (OCP) of 1.48 V with a peak power density of 153 mW $cm^{-2}$, significantly higher than the commercial Pt/C-based Zn-air battery (1.44 V, 119 mW $cm^{-2}$) (Fig. 5A, B). Besides, the specific capacity of FeCu SACs/NC-based Zn-air battery reached 741.9 mAh $g_{Zn}^{-1}$ with respect to the consumption of Zn anode, which was much larger than that of Pt/C (648.8 mAh $g_{Zn}^{-1}$) (Fig. 5C). Moreover, the as-assembled air battery based on the resultant FeCu SACs/NC catalyst exhibits excellent charge/discharge stability for a total of 280 cycles (Fig. 5D). Moreover, the assembled all-solid-state button-like Zn-air battery exhibits the high OCP of 1.44 V and the stable discharge platforms in various current density range with the good reproducibility after returning back to 0.1 mA $cm^{-2}$ (Fig. 5E, F), as well as good cyclic rechargeable stability at 0.2 mA $cm^{-2}$ for 14 h (Fig. 5G). The electrocatalytic oxygen evolution performance of FeCu SACs/NC and Pt/C were tested (Fig. S25), which exhibited the current density of 10 mA $cm^{-2}$ at the overpotential of 490 mV and 543 mV. The above results demonstrate that the FeCu SACs/NC possesses the potential of practical applications.

## 4. Conclusions

In summary, we reported a facile and effective method to fabricate dual-metal SACs consisting of atomically dispersed Fe and Cu species decorated with nitrogen-doped carbon matrix in the form of Fe-$N_4$ and Cu-$N_4$ coordination structures. The introduction of Cu-$N_4$ sites were verified from an experimental and theoretical perspective to playcrucial roles in optimizing the electronic structure of Fe-$N_4$ sites and accelerating the desorption of *OH intermediate process, as well as increasing the density of Fe active sites. Benefiting from the synergistic effects above, the resultant FeCu SACs/NC catalyst exhibited the comparable

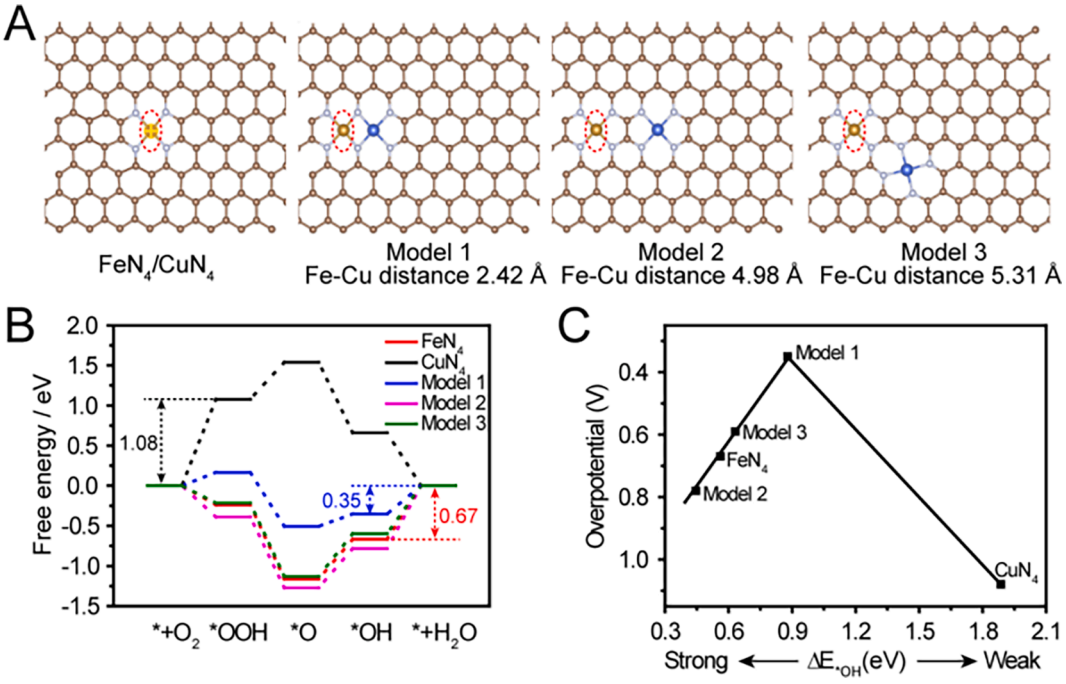


**Fig. 4.** (A) Structural models for Fe/Cu SACs/NC and FeCu SACs/NC, where the circled sites are the active sites for ORR. (B) Free energy diagram for ORR on the mononuclear site and binuclear site under the equilibrated potential U = 1.23 V. (C) Volcano plot of the ORR overpotential as a function of binding energy for immediate *OH. Color codes in the model are orange = Fe, blue = Cu, gray = N, bronze = C, respectively. (For interpretation of the references to color in this figure legend, the reader is referred to the web version of this article.)

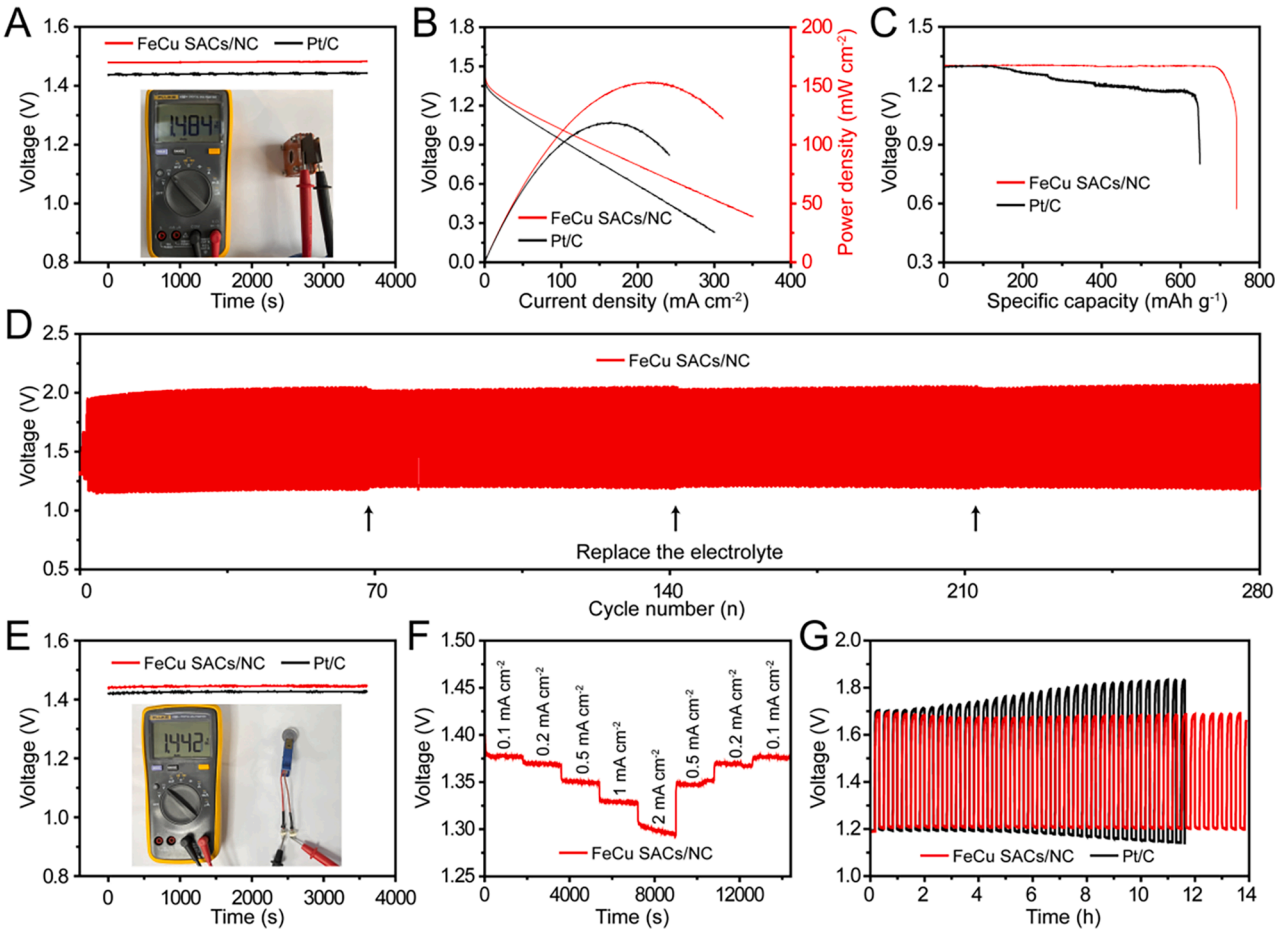


**Fig. 5.** (A) OCP curves, (B) LSV curves and power density curves, (C) discharging capacity curves,s (D) discharge and charge curves at the current density of 5 mA $cm^{-2}$ of the assembled Zn-air batteries based on the resultant FeCu SACs/NC as the air electrodes. (E) OCP curves, (F) discharge profiles at the different currents densities, (G) discharge and charge curves at the current density of 0.2 mA $cm^{-2}$ of the all-solid-state button-like Zn-air batteries.

ORR performance to Pt/C with the half-wave potential of 0.75 V and 0.89 V in 0.5 M $H_2SO_4$ and 0.1 M KOH. Moreover, the assemblled Zn-air batteries exhibited a high OCP of 1.48 V with a maximum power density of 153 mW $cm^{-2}$, outperforming the Pt/C (1.44 V, 119 mW $cm^{-2}$). Our work provides an effective strategy for the controllable construction of highly active sites for electrochemical energy devices.

## CRediT authorship contribution statement

**Heng Liu:** Methodology, Data curation, Formal analysis, Writing – original draft. **Luozhen Jiang:** Data curation, Formal analysis. **Yamin Wang:** Data curation, Formal analysis. **Xinxin Wang:** . **Javid Khan:** Writing – review & editing. **Yanlin Zhu:** . **Jiamin Xiao:** . **Lina Li:** Writing – review & editing. **Lei Han:** Supervision, Conceptualization, Writing – review & editing.

## Declaration of Competing Interest

The authors declare that they have no known competing financial interests or personal relationships that could have appeared to influence the work reported in this paper.

## Data availability

Data will be made available on request.

## Acknowledgements

This work is financially supported by Fundamental Research Funds for the Central Universities (No. 531118010232), Huxiang High-Level Talent Gathering Project of Hunan Province (No. 2019RS1012), National Key Basic Research Program of China (2017YFA0403402), Project of the National Natural Science Foundation of China (U1932119). We also acknowledge the support from Shanghai Large Scientific Facilities Centre and the staff from the 11B beamline at the Shanghai Synchrotron Radiation Facility (SSRF) for data collection.

## Appendix A. Supplementary data

Supplementary data to this article can be found online at https://doi.org/10.1016/j.cej.2022.138938.

## References

[1] C.X. Zhao, B.Q. Li, J.N. Liu, Q. Zhang, Intrinsic electrocatalytic activity regulation of M-N-C single-atom catalysts for the oxygen reduction reaction, Angew. Chem. Int. Ed. 59 (2020) 2–18.
[2] H.Y. Zhuo, X. Zhang, J.X. Liang, Q. Yu, H. Xiao, J. Li, Theoretical understandings of graphene-based metal single-atom catalysts: stability and catalytic performance, Chem. Rev. 120 (2020) 12315–12341.
[3] X.X. Wang, V. Prabhakaran, Y. He, Y. Shao, G. Wu, Iron-free cathode catalysts for proton-exchange-membrane fuel cells: cobalt catalysts and the peroxide mitigation approach, Adv. Mater. 31 (2019) e1805126.
[4] A.A. Gewirth, J.A. Varnell, A.M. DiAscro, Nonprecious metal catalysts for oxygen reduction in heterogeneous aqueous systems, Chem. Rev. 118 (5) (2018) 2313–2339.

[5] X.F. Yang, A. Wang, B. Qiao, J. Li, J. Liu, T. Zhang, Single-atom catalysts: a new frontier in heterogeneous catalysis, accounts of chemical research, Acc. Chem. Res. 46 (2013) 1740.

[6] W. Ma, H. Wan, L. Zhang, J.Y. Zheng, Z. Zhou, Single-atom catalysts for electrochemical energy storage and conversion, J. Energy Chem 63 (2021) 170–194.

[7] M. Tong, L. Wang, H. Fu, Designed synthesis and catalytic mechanisms of non-precious metal single-atom catalysts for oxygen reduction reaction, Small Methods 5 (10) (2021) e2100865.

[8] L. Peng, L.u. Shang, T. Zhang, G.I.N. Waterhouse, Recent advances in the development of single-Atom catalysts for oxygen electrocatalysis and zinc-air batteries, Adv. Energy Mater. 10 (48) (2020) 2003018.

[9] L. Cui, K. Fan, L. Zong, F. Lu, M. Zhou, B. Li, L. Zhang, L. Feng, X. Li, Y. Chen, L. Wang, Sol-gel pore-sealing strategy imparts tailored electronic structure to the atomically dispersed Ru sites for efficient oxygen reduction reaction, Energy Storage Mater. 44 (2022) 469–476.

[10] T. Sun, S. Mitchell, J. Li, P. Lyu, X. Wu, J. Pérez-Ramírez, J. Lu, Design of local atomic environments in single-atom electrocatalysts for renewable energy conversions, Adv. Mater. 33 (5) (2021) e2003075.

[11] B. Singh, V. Sharma, R.P. Gaikwad, P. Fornasiero, R. Zboril, M.B. Gawande, Single-atom catalysts: a sustainable pathway for the advanced catalytic applications, Small 17 (2021) e2006473.

[12] M. Primbs, Y. Sun, A. Roy, D. Malko, A. Mehmood, M.-T. Sougrati, P.-Y. Blanchard, G. Granozzi, T. Kosmala, G. Daniel, P. Atanassov, J. Sharman, C. Durante, A. Kucernak, D. Jones, F. Jaouen, P. Strasser, Establishing reactivity descriptors for platinum group metal (PGM)-free Fe-N-C catalysts for PEM fuel cells, Energy Environ. Sci. 13 (8) (2020) 2480–2500.

[13] M. Xiao, Y. Chen, J. Zhu, H. Zhang, X. Zhao, L. Gao, X. Wang, J. Zhao, J. Ge, Z. Jiang, S. Chen, C. Liu, W. Xing, Climbing the apex of the ORR volcano plot via binuclear site construction: electronic and geometric engineering, J. Am. Chem. Soc. 141 (2019) 17763–17770.

[14] Z. Zhu, H. Yin, Y. Wang, C.-H. Chuang, L. Xing, M. Dong, Y.-R. Lu, G. Casillas-Garcia, Y. Zheng, S. Chen, Y. Dou, P. Liu, Q. Cheng, H. Zhao, Coexisting single-atomic Fe and Ni sites on hierarchically ordered porous carbon as a highly efficient ORR electrocatalyst, Adv. Mater. 32 (42) (2020) e2004670.

[15] L. Gong, H. Zhang, Y. Wang, E. Luo, K. Li, L. Gao, Y. Wang, Z. Wu, Z. Jin, J. Ge, Z. Jiang, C. Liu, W. Xing, Bridge bonded oxygen ligands between approximated $FeN_4$ sites confer catalysts with high ORR performance, Angew. Chem. Int. Ed. 59 (33) (2020) 13923–13928.

[16] W. Zhu, Y. Pei, J.C. Douglin, J. Zhang, H. Zhao, J. Xue, Q. Wang, R. Li, Y. Qin, Y. Yin, D.R. Dekel, M.D. Guiver, Multi-scale study on bifunctional Co/Fe–N–C cathode catalyst layers with high active site density for the oxygen reduction reaction, Appl. Catal. B-Environ. 299 (2021), 120656.

[17] Y. Wu, C. Ye, L. Yu, Y. Liu, J. Huang, J. Bi, L. Xue, J. Sun, J. Yang, W. Zhang, X. Wang, P. Xiong, J. Zhu, Soft template-directed interlayer confinement synthesis of a Fe-Co dual single-atom catalyst for Zn-air batteries, Energy Storage Mater. 45 (2022) 805–813.

[18] X. Zhao, F. Wang, X.P. Kong, R. Fang, Y. Li, Dual-metal hetero-dingle-atoms with different coordination for efficient synergistic catalysis, J. Am. Chem. Soc. 143 (2021) 16068–16077.

[19] Y. Jia, X. Xiong, D. Wang, X. Duan, K. Sun, Y. Li, L. Zheng, W. Lin, M. Dong, G. Zhang, W. Liu, X. Sun, Atomically dispersed Fe-$N_4$ modified with precisely located S for highly efficient oxygen reduction, Nano-Micro Lett. 12 (2020) 116.

[20] K. Yuan, D. Lutzenkirchen-Hecht, L. Li, L. Shuai, Y. Li, R. Cao, M. Qiu, X. Zhuang, M.K.H. Leung, Y. Chen, U. Scherf, Boosting oxygen reduction of single iron active sites via geometric and electronic engineering: nitrogen and phosphorus dual coordination, J. Am. Chem. Soc. 142 (2020) 2404–2412.

[21] X. Feng, Y. Bai, M. Liu, Y. Li, H. Yang, X. Wang, C. Wu, Untangling the respective effects of heteroatom-doped carbon materials in batteries, supercapacitors and the ORR to design high performance materials, Energy Environ. Sci. 14 (4) (2021) 2036–2089.

[22] W. Wang, Q. Jia, S. Mukerjee, S. Chen, Recent insights into the oxygen-reduction electrocatalysis of Fe/N/C Materials, ACS Catal. 9 (11) (2019) 10126–10141.

[23] A. Kulkarni, S. Siahrostami, A. Patel, J.K. Nørskov, Understanding catalytic activity trends in the oxygen reduction reaction, Chem. Rev. 118 (5) (2018) 2302–2312.

[24] H. Yang, S. Gao, D. Rao, X. Yan, Designing superior bifunctional electrocatalyst with high-purity pyrrole-type $CoN_4$ and adjacent metallic cobalt sites for rechargeable Zn-air batteries, Energy Storage Mater. 46 (2022) 553–562.

[25] H. Yan, H. Cheng, H. Yi, Y. Lin, T. Yao, C. Wang, J. Li, S. Wei, J. Lu, Single-atom $Pd_1$/graphene catalyst achieved by atomic layer deposition: remarkable performance in selective hydrogenation of 1,3-butadiene, J. Am. Chem. Soc. 137 (2015) 10484–10487.

[26] M. Moses-DeBusk, M. Yoon, L.F. Allard, D.R. Mullins, Z. Wu, X. Yang, G. Veith, G. M. Stocks, C.K. Narula, CO Oxidation on supported single Pt atoms: experimental and ab initio density functional studies of CO interaction with Pt atom on θ-$Al_2O_3$(010) surface, J. Am. Chem. Soc. 135 (2013) 12634–12645.

[27] B. Qiao, A. Wang, X. Yang, L.F. Allard, Z. Jiang, Y. Cui, J. Liu, J. Li, T. Zhang, Single-atom catalysis of CO oxidation using $Pt_1/FeO_x$, Nat. Chem. 3 (8) (2011) 634–641.

[28] H. Tian, X. Cui, H. Dong, G. Meng, F. Kong, Y. Chen, L. Peng, C. Chen, Z. Chang, J. Shi, Engineering single $MnN_4$ atomic active sites on polydopamine-modified helical carbon tubes towards efficient oxygen reduction, Energy Storage Mater. 37 (2021) 274–282.

[29] X. Xie, L. Peng, H. Yang, G.I.N. Waterhouse, L.u. Shang, T. Zhang, MIL-101-Derived mesoporous carbon supporting highly exposed Fe single-atom sites as efficient oxygen reduction reaction catalysts, Adv. Mater. 33 (23) (2021) e2101038.

[30] Q. Wang, Y. Yang, F. Sun, G. Chen, J. Wang, L. Peng, W.T. Chen, L. Shang, J. Zhao, D. Sun-Waterhouse, T. Zhang, G.I.N. Waterhouse, Molten NaCl-assisted synthesis of porous Fe-N-C electrocatalysts with a high density of catalytically accessible $FeN_4$ active sites and outstanding oxygen reduction reaction performance, Adv. Energy Mater. 11 (2021) 2100219.

[31] F. Luo, A. Roy, L. Silvioli, D.A. Cullen, A. Zitolo, M.T. Sougrati, I.C. Oguz, T. Mineva, D. Teschner, S. Wagner, J.u. Wen, F. Dionigi, U.I. Kramm, J. Rossmeisl, F. Jaouen, P. Strasser, P-block single-metal-site tin/nitrogen-doped carbon fuel cell cathode catalyst for oxygen reduction reaction, Nat. Mater. 19 (11) (2020) 1215–1223.

[32] Z.-Y. Mei, S. Cai, G. Zhao, Q. Jing, X. Sheng, J. Jiang, H. Guo, Understanding electronic configurarions and coordination environment for enhanced ORR process and improved Zn-air battery performance, Energy Storage Mater. 50 (2022) 12–20.

[33] Y. Zhu, W. Sun, J. Luo, W. Chen, T. Cao, L. Zheng, J. Dong, J. Zhang, M. Zhang, Y. Han, C. Chen, Q. Peng, D. Wang, Y. Li, A cocoon silk chemistry strategy to ultrathin N-doped carbon nanosheet with metal single-site catalysts, Nat. Commun. 9 (2018) 3861.

[34] Z. Miao, X. Wang, M.C. Tsai, Q. Jin, J. Liang, F. Ma, T. Wang, S. Zheng, B.J. Hwang, Y. Huang, S. Guo, Q. Li, Atomically dispersed Fe-$N_x$/C Electrocatalyst boosts oxygen catalysis via a new metal-organic polymer supramolecule strategy, Adv. Energy Mater. 8 (2018) 1801226.

[35] S. Zhang, W. Yang, Y. Liang, X. Yang, M. Cao, R. Cao, T, Template-free synthesis of non-noble metal single-atom electrocatalyst with N-doped holey carbon matrix for highly efficient oxygen reduction reaction in zinc-air batteries, Appl. Catal. B-Environ. 285 (2021), 119780.

[36] J. Han, H. Bao, J.-Q. Wang, L. Zheng, S. Sun, Z.L. Wang, C. Sun, 3D N-Doped ordered mesoporous carbon supported single-atom Fe-N-C catalysts with superior performance for oxygen reduction reaction and zinc-air battery, Appl. Catal. B-Environ. 280 (2021), 119411.

[37] S.-H. Yin, J. Yang, Y.u. Han, G. Li, L.-Y. Wan, Y.-H. Chen, C. Chen, X.-M. Qu, Y.-X. Jiang, S.-G. Sun, Construction of highly active metal-containing nanoparticles and FeCo-$N_4$ composite sites for the acidic oxygen reduction reaction, Angew. Chem. Int. Ed. 59 (49) (2020) 21976–21979.

[38] C. Hu, H. Jin, B. Liu, L. Liang, Z. Wang, D. Chen, D. He, S. Mu, Propagating Fe-$N_4$ active sites with Vitamin C to efficiently drive oxygen electrocatalysis, Nano Energy 82 (2021), 105714.

[39] G. Yang, J. Zhu, P. Yuan, Y. Hu, G. Qu, B.A. Lu, X. Xue, H. Yin, W. Cheng, J. Cheng, W. Xu, J. Li, J. Hu, S. Mu, J.N. Zhang, Regulating Fe-spin state by atomically dispersed Mn-N in Fe-N-C catalysts with high oxygen reduction activity, Nat. Commun. 12 (2021) 1734.

[40] C.H. Choi, W.S. Choi, O. Kasian, A.K. Mechler, M.T. Sougrati, S. Brüller, K. Strickland, Q. Jia, S. Mukerjee, K.J.J. Mayrhofer, F. Jaouen, Unraveling the nature of sites active toward hydrogen peroxide reduction in Fe-N-C catalysts, Angew. Chem. Int. Ed. 56 (30) (2017) 8809–8812.

[41] L. Zhang, S. Jiang, W. Ma, Z. Zhou, Oxygen reduction reaction on Pt-based electrocatalysts: Four-electron vs. two-electron pathway, Chinese, J. Catal. 43 (2022) 1433–1443.

[42] M. Tong, F. Sun, Y. Xie, Y. Wang, Y. Yang, C. Tian, L. Wang, H. Fu, Operando cooperated catalytic mechanism of atomically dispersed Cu-$N_4$ and Zn-$N_4$ for promoting oxygen reduction reaction, Angew. Chem. Int. Ed. 60 (25) (2021) 14005–14012.

[43] A. Serov, M.H. Robson, M. Smolnik, P. Atanassov, Templated bi-metallic non-PGM catalysts for oxygen reduction, Electrochim. Acta 80 (2012) 213–218.

[44] Q. Zhang, P. Kumar, X. Zhu, R. Daiyan, N.M. Bedford, K.H. Wu, Z. Han, T. Zhang, R. Amal, X. Lu, Electronically modified atomic sites within a multicomponent Co/Cu composite for efficient oxygen electroreduction, Adv. Energy Mater. 11 (2021) 2100303.

[45] C. Zhu, Q. Shi, B.Z. Xu, S. Fu, G. Wan, C. Yang, S. Yao, J. Song, H. Zhou, D. Du, S. P. Beckman, D. Su, Y. Lin, Hierarchically porous M-N-C (M = Co and Fe) single-atom electrocatalysts with robust $MN_x$ active moieties enable enhanced ORR performance, Adv. Energy Mater. 8 (2018) 1801956.

[46] L. Yan, L. Xie, X.-L. Wu, M. Qian, J. Chen, Y. Zhong, Y. Hu, Precise regulation of pyrrole-type single-atom Mn-$N_4$ sites for superior pH-universal oxygen reduction, Carbon, Energy 3 (6) (2021) 856–865.

[47] W. Xie, J. Li, Y. Song, S. Li, J. Li, M. Shao, Hierarchical carbon microtube@ nanotube core–shell structure for high-performance oxygen electrocatalysis and Zn–air battery, Nano-Micro Lett. 12 (2020) 97.

[48] Q. Shi, Y. He, X. Bai, M. Wang, D.A. Cullen, M. Lucero, X. Zhao, K.L. More, H. Zhou, Z. Feng, Y. Liu, G. Wu, Methanol tolerance of atomically dispersed single metal site catalysts: mechanistic understanding and high-performance direct methanol fuel cells, Energy Environ. Sci. 13 (2020) 3544–3555.

[49] Y. Qu, L. Wang, Z. Li, P. Li, Q. Zhang, Y. Lin, F. Zhou, H. Wang, Z. Yang, Y. Hu, M. Zhu, X. Zhao, X. Han, C. Wang, Q. Xu, L. Gu, J. Luo, L. Zheng, Y. Wu, Ambient synthesis of single-atom catalysts from bulk metal via trapping of atoms by surface dangling bonds, Adv. Mater. 31 (44) (2019) 1904496.

[50] J. Frédéric, L. Michel, D. Jean-Pol, C. Mei, Heat-treated Fe/N/C catalysts for $O_2$ electroreduction: are active sites hosted in micropores? J. Phys. Chem. B 110 (2006) 5553–5558.

[51] X. Li, L.u. Ni, J. Zhou, L. Xu, C. Lu, G. Yang, W. Ding, W. Hou, Encapsulation of Fe nanoparticles into an N-doped carbon nanotube/nanosheet integrated hierarchical architecture as an efficient and ultrastable electrocatalyst for the oxygen reduction reaction, Nanoscale 12 (26) (2020) 13987–13995.

[52] L. Jiao, R. Zhang, G. Wan, W. Yang, X. Wan, H. Zhou, J. Shui, S.-H. Yu, H.-L. Jiang, Nanocasting $SiO_2$ into metal–organic frameworks imparts dual protection to high-loading Fe single-atom electrocatalysts, Nat. Commun. 11 (2020) 2831.

[53] Y. Zhou, X. Tao, G. Chen, R. Lu, D. Wang, M.X. Chen, E. Jin, J. Yang, H.W. Liang, Y. Zhao, X. Feng, A. Narita, K. Mullen, Multilayer stabilization for fabricating high-loading single-atom catalysts, Nat. Commun. 11 (2020) 5892.
[54] Y. Wang, X. Cui, L. Peng, L. Li, J. Qiao, H. Huang, J. Shi, Metal-nitrogen-carbon catalysts of specifically coordinated configurations toward typical electrochemical redox reactions, Adv. Mater. 33 (34) (2021) e2100997.
[55] Y.-W. Li, W.-J. Zhang, J. Li, H.-Y. Ma, H.-M. Du, D.-C. Li, S.-N. Wang, J.-S. Zhao, J.-M. Dou, L. Xu, Fe-MOF-Derived efficient ORR/OER bifunctional electrocatalyst for rechargeable zinc-air batteries, ACS Appl. Mater. Interfaces 12 (40) (2020) 44710–44719.
[56] L. Wang, L. Zhang, W. Ma, H. Wan, X. Zhang, X. Zhang, S. Jiang, J.Y. Zheng, Z. Zhou, In situ anchoring massive isolated Pt atoms at cationic vacancies of α-$Ni_xFe_{1-x}(OH)_2$ to regulate the electronic structure for overall water splitting, Adv. Funct. Mater. 32 (2022) 2203342.
[57] Y. Qu, Z. Li, W. Chen, Y. Lin, T. Yuan, Z. Yang, C. Zhao, J. Wang, C. Zhao, X. Wang, F. Zhou, Z. Zhuang, Y. Wu, Y. Li, Direct transformation of bulk copper into copper single sites via emitting and trapping of atoms, Nat. Catal. 1 (10) (2018) 781–786.
[58] N. Zhang, T. Zhou, M. Chen, H.u. Feng, R. Yuan, C. Zhong, W. Yan, Y. Tian, X. Wu, W. Chu, C. Wu, Y.i. Xie, Xie, High-purity pyrrole-type $FeN_4$ sites as a superior oxygen reduction electrocatalyst, Energy Environ. Sci. 13 (1) (2020) 111–118.
[59] N. Zhang, T. Zhou, J. Ge, Y. Lin, Z. Du, C. Zhong, W. Wang, Q. Jiao, R. Yuan, Y. Tian, W. Chu, C. Wu, Y.i. Xie, Xie, High-density planar-like $Fe_2N_6$ structure catalyzes efficient oxygen reduction, Matter 3 (2) (2020) 509–521.
[60] T. Wang, C. Yang, Y. Liu, M. Yang, X. Li, Y. He, H. Li, H. Chen, Z. Lin, Dual-shelled multidoped hollow carbon nanocages with hierarchical porosity for high-performance oxygen reduction reaction in both alkaline and acidic media, Nano Lett. 20 (8) (2020) 5639–5645.
[61] D. Li, Y.i. Jia, G. Chang, J. Chen, H. Liu, J. Wang, Y. Hu, Y. Xia, D. Yang, X. Yao, A defect-driven metal-free electrocatalyst for oxygen reduction in acidic electrolyte, Chem 4 (10) (2018) 2345–2356.
[62] D. Xia, X. Yang, L. Xie, Y. Wei, W. Jiang, M. Dou, X. Li, J. Li, L. Gan, F. Kang, Direct growth of carbon nanotubes doped with single atomic Fe–$N_4$ active dites and neighboring graphitic nitrogen for efficient and stable oxygen reduction electrocatalysis, Adv. Funct. Mater. 29 (2019) 1906174.